Model-based autofocus for near-field phase retrieval

Johannes Dora,[1,2,*] Martin Möddel,[1,3] Silja Flenner,[4] Jan Reimers,[5,6] Berit Zeller-Plumhoff,[5,7] Christian G. Schroer,[2,8,9] Tobias Knopp,[1,3,10] and Johannes Hagemann[2]

[1]*Institute for Biomedical Imaging, University of Technology Hamburg TUHH, Lottestr. 55, 22529 Hamburg, Germany*
[2]*Centre for X-ray and Nano Science CXNS, Deutsches Elektronen-Synchrotron DESY, Notkestr. 85, 22607 Hamburg, Germany*
[3]*Section for Biomedical Imaging, University Medical Center Hamburg-Eppendorf UKE, Lottestr. 55, 22529 Hamburg, Germany*
[4]*Institute of Materials Physics, Helmholtz-Zentrum Hereon, Max-Planck-Str. 1, 21502 Geesthacht, Germany*
[5]*Institute of Metallic Biomaterials, Helmholtz-Zentrum Hereon, Max-Planck-Str. 1, 21502 Geesthacht, Germany*
[6]*Ernst Ruska-Centre for Microscopy and Spectroscopy with Electrons, Forschungszentrum Jülich GmbH, Jülich 52425, Germany*
[7]*Faculty of Mechanical Engineering and Marine Technologies, University of Rostock, Albert-Einstein-Straße, 218059 Rostock, Germany*
[8]*Department Physik, Universität Hamburg UHH, Luruper Chaussee 149, 22761 Hamburg, Germany*
[9]*Helmholtz Imaging, Deutsches Elektronen-Synchrotron DESY, Notkestr. 85, 22607 Hamburg, Germany*
[10]*Fraunhofer Research Institution for Individualized and Cell-based Medical Engineering IMTE, Mönkhofer Weg 239a, 23562 Lübeck, Germany*
*johannes.dora@desy.de

Abstract: The phase problem is a well known ill-posed reconstruction problem of coherent lens-less microscopic imaging, where only the intensities of a complex wave-field are measured by the detector and the phase information is lost. For the reconstruction of sharp images from holograms in a near-field experimental setting, it is crucial to solve the autofocus problem, i.e., to precisely estimate the Fresnel number of the forward model. Otherwise, blurred out-of focus images that also can contain artifacts are the result. In general, a simple distance measurement at the experiment is not sufficiently accurate, thus the fine-tuning of the Fresnel number has to be done prior to the actual reconstructions. This can be done manually or automatically by an estimation algorithm. To automatize the process, as needed, e.g., for *in-situ/operando* experiments, different focus criteria have been widely studied in literature but are subjected to certain restrictions. The methods often rely on image analysis of the reconstructed image, making them sensitive to image noise and also neglecting algorithmic properties of the applied phase retrieval. In this paper, we propose a novel criterion, based on a model-matching approach, which improves autofocusing by also taking the underlying reconstruction algorithm, the forward model and the measured hologram into account. We derive a common autofocusing framework, based on a recent phase-retrieval approach and a downhill-simplex method for the automatic optimization of the Fresnel number. We further demonstrate the robustness of the framework on different data sets obtained at the nano imaging endstation of P05 at PETRA III (DESY, Hamburg) operated by Helmholtz-Zentrum Hereon.

1. Introduction

The autofocus problem is a widely known problem in imaging systems and and has already been studied in literature, especially in the field of optical microscopy [1–8]. In near-field holography (NFH) with hard X rays as sketched in Fig. 1, the autofocus problem is part of the phase problem, where only the intensity of a complex wave-field is measured by a detector while the phase information is lost [9–13]. For the reconstruction of sharp images of the measured objects, the forward model has to be parameterized very precisely. Otherwise, reconstructions will generate artifacts or result in a loss of resolution. An example is shown in Fig. 2. In digital holography applications [14–17], illumination wavelength and the setup geometry are often summarized into a common scalar, the Fresnel number. However, due to various limitations, an accurate Fresnel number cannot always easily be determined and has to be fine tuned in a time-consuming process before the actual reconstruction. Due to the development towards more routine NFH measurements, the amount of data also increases. Thus, fast reconstruction algorithms and an automatic optimization of the Fresnel number becomes a necessity. This is especially relevant for *in-situ/operando* studies [18–22] at synchrotron radiation facilities with X ray microscopy setups [23]. With further progress in the development of experimental hardware and reconstruction algorithms, the complexity of measured objects continuously increases. Recent developments in lens-less X-ray near-field holography enable the measurement of strong interacting objects and directly reconstruct the projected refractive index of an object from a single hologram [27] without a spatial support constraint [28]. The Fresnel number has to be optimized from noisy holograms for mixed phase- and absorption contrast images.
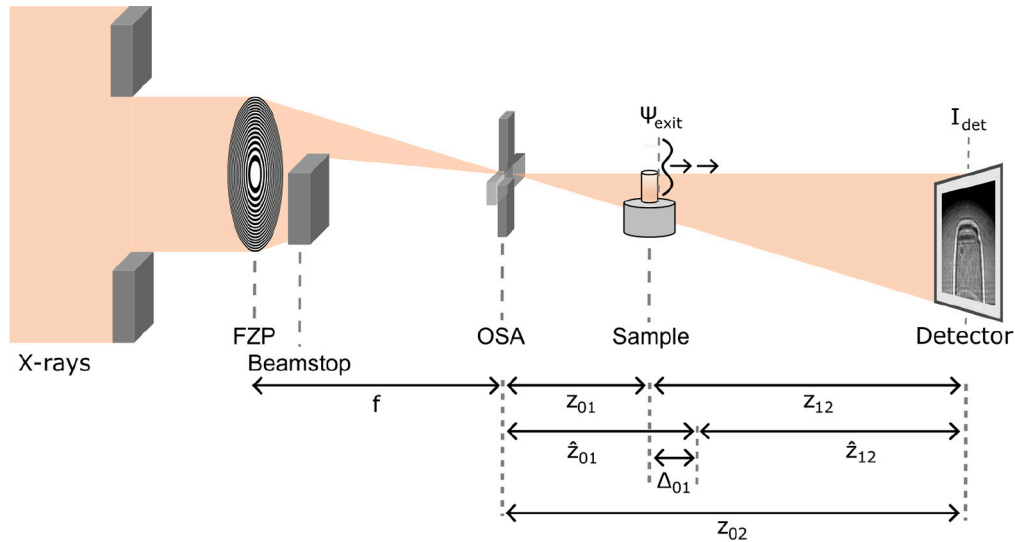

Fig. 1. Sketch of an experimental setup based on a Fresnel zone plate for near-field holographic microscopy [23]. The distances are measured from the focal point of the optics, located at f. The distance of the detector z_{02} is assumed to be known. The exit wave-field ψ_{exit} is propagated by the distance z_{12} to the detector, where only its squared magnitude is measured, which yields the hologram $\mathcal{I}_{\text{det}}$. A perturbation in z_{01} by Δ_{01} in the assumed forward model yields new values $\hat{z}_{01}$ and $\hat{z}_{12}$. It changes the cone-beam geometry of the forward model and the effective propagation distance in the equivalent parallel beam.

The required robustness of a numerical focus-error metric challenges autofocus approaches. Different error metrics to quantify the de-focus have been widely studied in literature, however either with certain object assumptions, a manual selection of a region of interest or under
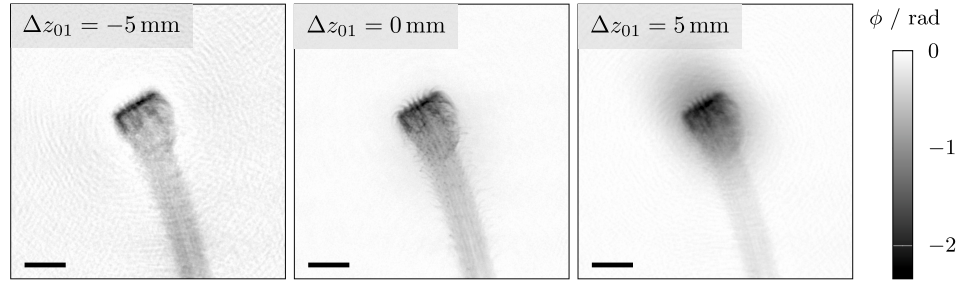
Fig. 2. Reconstructed phase images of a spider attachment hair [24–26] for correct and de-focused focus-object distances z_{01} in the forward model (Fig. 1) of the reconstruction: $-5\,\text{mm}$ de-focused (left), in focus (middle), $+5\,\text{mm}$ de-focused (right). The scale bars indicate $8\,\mu\text{m}$.

different experimental conditions. Metrics from literature that we will compare in this paper for single-distance X-ray near-field holography experiments are the image variance measure VAR [1,7], an analysis of weighted base functions SPEC [1,5,6], a statistical analysis of the gradient of first order GRA [1,4,7], and the second order gradient or Laplacian LAP [1,4,7] and two gradient sparsity measures, the Tamura coefficient of the gradient and the Gini index of the gradient, ToG and GoG [2,8,29]. These methods rely exclusively on the analysis of the reconstructed object $\tilde{\text{O}}$, making them sensitive to reconstruction artifacts that may be induced by the underlying algorithm. The behavior of metrics may therefore change between reconstruction algorithms, which is rarely considered in the literature. In this paper, we propose a novel focus criterion based on a model fit error (MFE). We derive the theoretical concept of this metric that includes the reconstructed image, the forward model and the measured hologram into the error quantification. Eventually, we derive a common autofocus framework, based on the downhill-simplex method for the automatic optimization of the Fresnel number and demonstrate the robustness of our approach on experimental data, obtained at the nano imaging endstation of P05 at PETRA III (DESY, Hamburg) operated by Helmholtz-Zetrum Hereon [30–32]. The data and the software underlying the results presented in this paper are available in Code 1, Ref. [33].

2. Problem statement

We assume a measurement setup according to Fig. 1 under the projection approximation for measured objects [27,28,34] with thickness d. The measured sample is described in terms of projected complex refractive indices

$$\tilde{\text{O}}(x,y) := -k \int_0^d \delta(x,y,z) - i\,\beta(x,y,z)\,dz = \phi(x,y) + i\,\mu(x,y), \tag{1}$$

where δ and ϕ encode the dispersion, i.e., phase shifting properties of the object and β and μ the attenuation, i.e., absorption properties of the object. The number $k = 2\pi/\lambda$ is the wave number of the illumination. In the following, we omit the spatial coordinates (x,y) for readability. The propagation of the exit wave-field

$$\psi_{\text{exit}}(\tilde{\text{O}}) = \exp(i\,\tilde{\text{O}}), \tag{2}$$

behind the object to the detector is then described by the free-space Fresnel propagation. $\mathcal{D}_{\text{Fr}}^z(\tilde{\text{O}})$ describes the propagation over a distance z with

$$\mathcal{D}_{\text{Fr}}^z(\tilde{\text{O}}) := \mathcal{F}^{-1} \circ \exp\left(-i \cdot \pi \frac{(k_x^2 + k_y^2)}{\text{Fr}(z)}\right) \circ \mathcal{F} \circ \psi_{\text{exit}}(\tilde{\text{O}}). \tag{3}$$

The Fresnel number summarizes the setup parameters into a scalar number. For a parallel beam setup, it is a function $\mathrm{Fr}(z)$ of the propagation distance z with

$$\mathrm{Fr}(z) = \frac{(\Delta x)^2}{\lambda z}, \tag{4}$$

where Δx is the pixel size and λ is the wavelength of the illumination. To transform the cone-beam of Fig. 1 into an equivalent parallel beam, we need two magnification factors M_1 and M_2, rescaling the pixel size and the propagation distance respectively, according to the Fresnel scaling theorem [34]. In the setup of Fig. 1, the cone-beam geometry is determined by the two distances z_{01} and $z_{02} = z_{01} + z_{12}$ and the physical dimension of the detector pixels, i.e., the pixel size Δx. The Fresnel number $\mathrm{Fr}(z)$ for this geometry and a propagation distance z with respect to the sample is then given by

$$\mathrm{Fr}(z) = \frac{(\Delta x/M_1)^2}{\lambda(z/M_2)}, \tag{5}$$

with the magnification factors

$$M_1 = \frac{z_{02}}{z_{01}}, \tag{6}$$

$$M_2 = \frac{z_{01} + z}{z_{01}}, \tag{7}$$

where M_1 is the magnification between the sample and the detector plane and M_2 is the magnification between the sample and the plane at the propagation distance z. In the following, we assume an experimental condition, where the distance z_{01} is only known within a measurement uncertainty $\Delta_M = \pm 5\,\mathrm{mm}$. A single hologram is acquired and the complex refractive indices are retrieved as a projection image. The reconstruction is performed by the phase retrieval algorithm of [28]. Figure 3 shows the impact of a perturbation in z_{01} by Δ_{01} and a perturbation in z_{02} by Δ_{02} on the Fresnel number Fr. The values are plotted as the relative change of Fr in percent with the function

$$\mathrm{ERR}(\hat{\mathrm{Fr}}_{\mathrm{det}}) := \left| \frac{\hat{\mathrm{Fr}}_{\mathrm{det}}}{\mathrm{Fr}_{\mathrm{det}}} - 1 \right|, \tag{8}$$

where $\mathrm{Fr}_{\mathrm{det}}$ is the correct and $\hat{\mathrm{Fr}}_{\mathrm{det}}$ is the distorted Fresnel number. While small errors in z_{02} have a negligible impact, an error of $\pm 5\,\mathrm{mm}$ for the z_{01} value changes the forward model significantly and results in a blurry reconstruction of the phase values. The appearance of fringe artifacts in the reconstructed phase images, as shown in Fig. 2, are caused by a mismatch between the numerical focus of the reconstruction and the experiment. To optimize the Fresnel number, we therefore aim to refine the distance z_{01} before a reconstruction of $\tilde{O}$ is performed.

A straight forward way to retrieve a more accurate value for z_{01} is to reconstruct an image series with different values for the Fr and eventually choose the visual most appealing result, in the sense of image sharpness. However, this approach is time consuming and entails a high demand of computational resources. This makes a manual method impractical for certain applications like time sensitive *in-situ/operando* measurements.

We therefore seek an algorithm that is capable of automatically finding the focus-sample distance z_{01} for a NFH setup as shown in Fig. 1. The method needs to be robust for a large variety of measured objects, under *in-situ/operando* conditions and a high level of noise in the data. To this end, an error metric needs to be found that is capable of quantifying the de-focus of the reconstructed result. From this metric, an optimization problem and its solver have to be derived, which will be the subject of the next section.
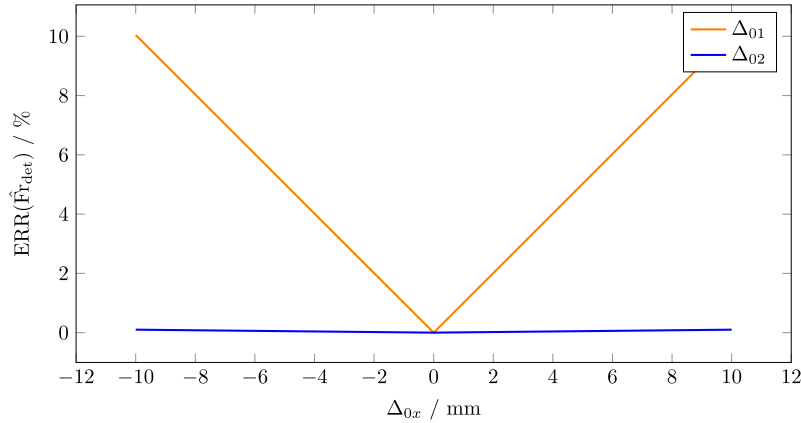
Fig. 3. Comparison of the impact of an inaccuracy Δ_{01} in z_{01} (orange) and Δ_{02} in z_{02} (blue) on the Fresnel number Fr in the range of ± 5 mm. The relative change of Fr is plotted in percent over the aberration in mm. While small errors in z_{02} have a negligible impact inaccuracies in the z_{01} value change the Fresnel number and consequently the forward model significantly.

3. Methods

3.1. Model fit error (MFE) metric for de-focus quantification

We propose a novel focus criterion which aims to quantify the de-focus of a de-focused wave-field $\hat{\psi}$. The quantification is performed by a data-driven approach which measures the fitting of the forward model Eq. (3), that is used, e.g., in a phase retrieval algorithm for the propagation from the object plane to the detector plane. In the following, we define $\hat{z}_{01}$, which is the correct distance z_{01} of the measurement setup plus a de-focus Δ_{01}:

$$\hat{z}_{01} = z_{01} + \Delta_{01}, \tag{9}$$

and consequently for the object-detector distance $\hat{z}_{12}$ with the introduced de-focus Δ_{01}:

$$\hat{z}_{12} = z_{12} - \Delta_{01}. \tag{10}$$

The parameters are shown in Fig. 1. The de-focused wave-field $\hat{\psi}$ can be expressed by a Fresnel-propagation of the in-focus wave-field ψ_{exit} to the de-focus-position Δ_{01}. The result is $\hat{\psi}$ with:

$$\hat{\psi} = \mathcal{D}_{\text{Fr}}^{\Delta_{01}}(\psi_{\text{exit}}). \tag{11}$$

We know that the values of ψ_{exit} cannot exceed a certain range. The range is given by the non-negative electron density constraint Ω_P that states the following: Under X-ray illumination, the object in the beam is only negatively phase shifting and does not add intensity. Mathematically, the constraint Ω_P for a wave-field ψ is expressed as

$$\Omega_P = \{x \in \psi : \arg(x) \in [-\infty, 0], \ |x| \in [0, 1]\}. \tag{12}$$

We utilize the property of the constraint Ω_P that it is only accurate for an in-focus wave-field ψ_{exit} and invalid for a de-focused wave-field $\hat{\psi}$. A de-focused wave-field contains always fringes with values outside of Ω_P. The more de-focused $\hat{\psi}$ is, the stronger the fringes are. Applying a projector $\mathcal{P}f_{\Omega_P}$ on $\hat{\psi}$ eliminates these values and thereby makes it impossible to recover ψ_{exit} by

propagation:

$$\hat{\psi}_P = \mathcal{P}_{\Omega_P} \hat{\psi}. \tag{13}$$

Instead, we obtain a projected wave-field that is inconsistent with respect to a measured hologram $\mathcal{I}_{\text{det}}$ that corresponds to ψ_{exit}. We can quantify how inconsistent the values of $\hat{\psi}_P$ are with respect to $\mathcal{I}_{\text{det}}$ by calculating the mean squared error MSE. The mean squared error of $\hat{\psi}_P$ is given by a propagation to the detector plane at distance $\hat{z}_{12}$ and then by comparing the magnitudes. We introduce the term model fit error (MFE), which is the MSE of a $\hat{\psi}_P$. It is given by

$$\text{MFE} = \left\lVert \left\lvert \mathcal{D}_{\text{Fr}}^{-\Delta_{01}} \left(\mathcal{D}_{\text{Fr}}^{z_{12}} \left(\mathcal{P}_{\Omega_P} \mathcal{D}_{\text{Fr}}^{\Delta_{01}} \left(\psi_{\text{exit}} \right) \right) \right) \right\rvert - \sqrt{\mathcal{I}_{\text{det}}} \right\rVert_2^2. \tag{14}$$

We evaluate the behavior of MFE criterion empirically for different objects in a simulation in Sec. 4. Phase-retrieval algorithms that use a forward model with wrong distances $\hat{z}_{01}$ and $\hat{z}_{12}$ will reconstruct de-focused values as shown in Fig. 2, which means, e.g., $\hat{\psi}$ or $\hat{\psi}_P$. If only the distance with de-focus $\hat{z}_{12}$ and the de-focused, projected wave-field $\hat{\psi}_P$ are known, Eq. (14) becomes simply:

$$\text{MFE} = \left\lVert \left\lvert \mathcal{D}_{\text{Fr}}^{\hat{z}_{12}} \left(\hat{\psi}_P \right) \right\rvert - \sqrt{\mathcal{I}_{\text{det}}} \right\rVert_2^2. \tag{15}$$

The concept of maximizing the data consistency to find the correct distance can also be found in ptychography with multi-slicing [35,36], where ψ_{exit} is directly reconstructed in the correct in-focus plane.

3.2. Global optimization problem for z_{01}

In the following, we propose an algorithm for the automatic refinement of the distance z_{01} in Fig. 1 in the forward model, based on the optimization of a global inverse problem. We are aiming to find an approximated solution $z_{01}{}^*$ of the general optimization problem:

$$z_{01}{}^* = \underset{\hat{z}_{01} \in \Omega_z}{\operatorname{argmin}} f(\hat{z}_{01}), \tag{16}$$

with a constraint Ω_z on the estimate z_{01} under an initial guess z_{01}^{est} and the measurement uncertainty Δ_{M}:

$$\Omega_z = \left\{ x : x \in \mathbb{R}, \ x \in [z_{01}^{\text{est}} - \Delta_{\text{M}}, z_{01}^{\text{est}} + \Delta_{\text{M}}] \right\}. \tag{17}$$

The function $f(\hat{z}_{01})$ is a general error metric or distance function that quantifies the de-focus with respect to the correct value z_{01}. The function $f(\hat{z}_{01})$ should have (i) its minimum at $\hat{z}_{01} = z_{01}$ and (ii) increasing function values with increasing distance from the optimum. We split $f(\hat{z}_{01})$ further into two nested functions $\mathcal{G}$ and $\tilde{\text{O}}$:

$$z_{01}{}^* = \underset{\hat{z}_{01} \in \Omega_z}{\operatorname{argmin}} \mathcal{G}(\tilde{\text{O}}(\hat{z}_{01})), \tag{18}$$

where $\tilde{\text{O}}(\hat{z}_{01})$ is the representation of the projected refractive indices $\tilde{\text{O}}$ of Eq. (1) that corresponds to the respective wave-field $\hat{\psi}_P$ for a given position $\hat{z}_{01}$ in the sense of

$$\tilde{\text{O}}(\hat{z}_{01}) \mapsto \hat{\psi}_P = \exp\left(\mathrm{i}\, \tilde{\text{O}}(\hat{z}_{01})\right). \tag{19}$$

Because the two functions $\mathcal{G}$ and $\tilde{\text{O}}(\hat{z}_{01})$ are nested, there is an implicit interdependence between the error metric and the method to retrieve $\tilde{\text{O}}$. The function $\mathcal{G}$ will rely on abstract features of $\tilde{\text{O}}$, which, under variations of $\hat{z}_{01}$, must be reliably and self-consistently produced by the reconstruction to satisfy requirements (i) and (ii).

3.3.   Retrieval of Õ

In the following, we introduce shortly the reconstruction method for Õ that we used to test the MFE criterion with experimental data. The respective hyper-parameters have been empirically determined and are shown in the Appendix in Table 3. The parameters have been optimized with respect to the reconstruction speed and consistency over different $\hat{z}_{01}$ values. We evaluate the behavior of MFE criterion empirically for different experimental datasets in Sec. 4.

The solution of the underlying optimization problem for the retrieval of $\tilde{O}(\hat{z}_{01})$ is based on the ASRM algorithm of [28]. We parameterized the Fresnel propagator Eq. (3) with the estimate $\hat{z}_{01}$. The reconstruction algorithm optimizes the target function

$$\tilde{O}^*(\hat{z}_{01}) = \underset{\tilde{O} \in \Omega_P}{\mathrm{argmin}} \; \frac{1}{2} \| \mathcal{D}_{\mathrm{Fr}}^{z_{02}-\hat{z}_{01}}(\tilde{O}) - \sqrt{S_\downarrow \mathcal{I}_{\mathrm{det}}} + \|_2^2 + \beta \| \mathrm{Im}(\tilde{O}) \|_2 = \underset{\tilde{O} \in \Omega_P}{\mathrm{argmin}} \; \mathcal{L}(\tilde{O}, \hat{z}_{01}), \quad (20)$$

under the constraint set

$$\Omega_P = \left\{ x \in \tilde{O} : \mathrm{Re}(x) \in [-\infty, 0], \; \mathrm{Im}(x) \in [-\log(A_0), \infty] \right\}, \quad (21)$$

where the symbol A_0 is an intensity offset correction. Note that Eq. (21) is the refractive version of Eq. (12), which can be applied without having to consider phase-wrapping issues. We performed the reconstruction with a multi-grid approach with the down-sampling operator $S_\downarrow$. We further stabilized the reconstruction with an L_2-regularization applied on the absorption values.

3.4.   Automatic optimization of the global optimization problem for z_{01}

Optimization problems such as Eq. (18) are typically solved with iterative algorithms. While it is in principle possible to optimize Õ and $\hat{z}_{01}$ simultaneously [37,38], this is not straightforward for single-distance X-ray near-field holography, where the experimental conditions are not as well defined as in visible light holography with weakly interacting samples. The reconstruction of Õ is already highly ill-posed without an additional optimization parameter. To separate both optimization problems, we define a nested optimization problem from a combination of Eq. (18) and Eq. (20) with

$$z_{01}^* = \underset{\hat{z}_{01} \in \Omega_z}{\mathrm{argmin}} \; \mathcal{G} \left(\underset{\tilde{O} \in \Omega_P}{\mathrm{argmin}} \; \mathcal{L}(\tilde{O}, \hat{z}_{01}) \right). \quad (22)$$

Since the gradient of $\mathcal{G}$ is not trivially accessible, we therefore optimize function $\mathcal{G}$ of Eq. (22) numerically with a downhill simplex method. The downhill simplex method, also known as the Nelder-Mead method, is a gradient-less algorithm to optimize a multivariate objective function, which can also be non-linear [39,40]. The objective function is sampled by corner points of a multidimensional simplex, which shrinks with each iteration towards a minimum. In each probing point, the inner optimization problem has to be solved, i.e., a reconstruction of Õ has to be performed. The constraint Ω_z can be simply implemented by a projection of the corner points on the valid interval defined by Ω_z. If the size of the simplex falls below a predefined threshold, the algorithm stops. Fig. 4 visualizes how the simplex algorithm traverses an ideal and a noisy function. The graphs were generated by applying the Nelder-Mead algorithm on a simulated parabolic function without and with additive noise.

3.5.   Simulation setup

To evaluate the MFE error metric, we first created three different phantoms (Fig. 5) that aim to cover different classes of object complexity: A triangle with strong edges in combination with a smooth surface. A biological cell with lot of small and sharp features. A ball, covering a wide range of image gradients. The created phantoms are mixed objects, phase shifting and absorbing. The phantoms are simulated as single material objects with a fixed δ/β relationship.
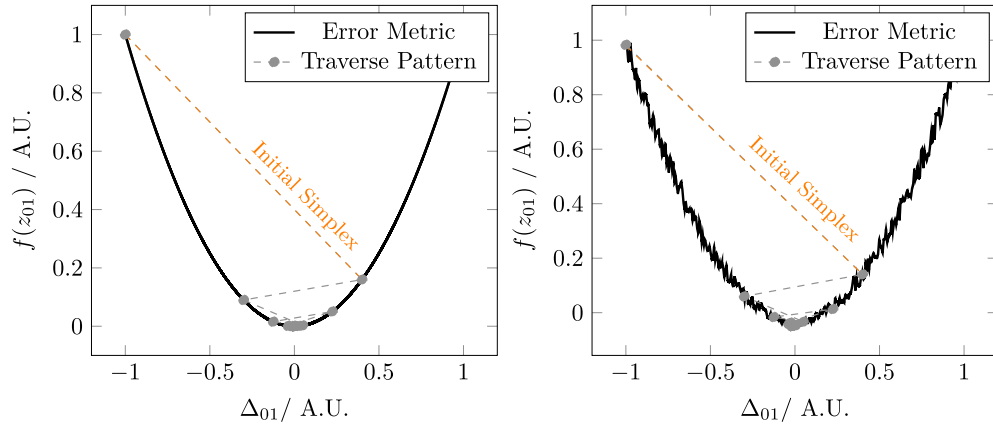
Fig. 4. The Nelder-Mead method applied to an ideal and noisy function. Left: Demonstration of the underlying principle. The method traverses a function by probing single points. The first two connected points create an initial simplex that shrinks over time. After some iterations, the method reaches a minimum. The algorithm terminates when a certain predefined simplex length is reached. Right: Demonstration of the behavior in the presence of noise. It can be seen that although the function is corrupted, the Nelder-Mead method traverses a similar path towards the minimum. This is supported by the probing method instead of calculating a gradient.

For each phantom $\tilde{O}$, we sampled 201 $\hat{z}_{01}$ in the interval of $[z_{01}^0 - 2\Delta_M, \ z_{01}^0 + 2\Delta_M]$, where z_{01}^0 is the ground truth and Δ_M is the expected measurement uncertainty. For each sampling point, we calculated the corresponding $\hat{\psi}$ by propagating the ground-truth wave-field ψ_{exit} to a de-focus position with Eq. (11). We further applied the constraint Ω_P of Eq. (12) to retrieve $\hat{\psi}_P$ of Eq. (13). The $\hat{\psi}_P$ results are used as an input for each error metric. For the MFE criterion, we assumed a noise-free and flat-field correction artifact free hologram.
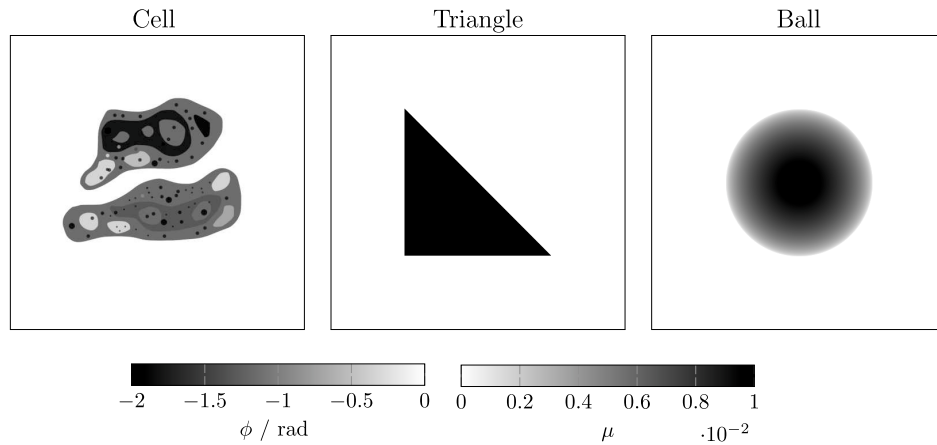

Fig. 5. Simulated objects. The simulated objects are mixed objects, phase shifting (ϕ) and absorbing (μ) according to the color bars. We created the following shapes: A triangle with strong edges in combination with a smooth surface, a biological cell with lot of small and sharp features, ball covering a wide range of image gradients.
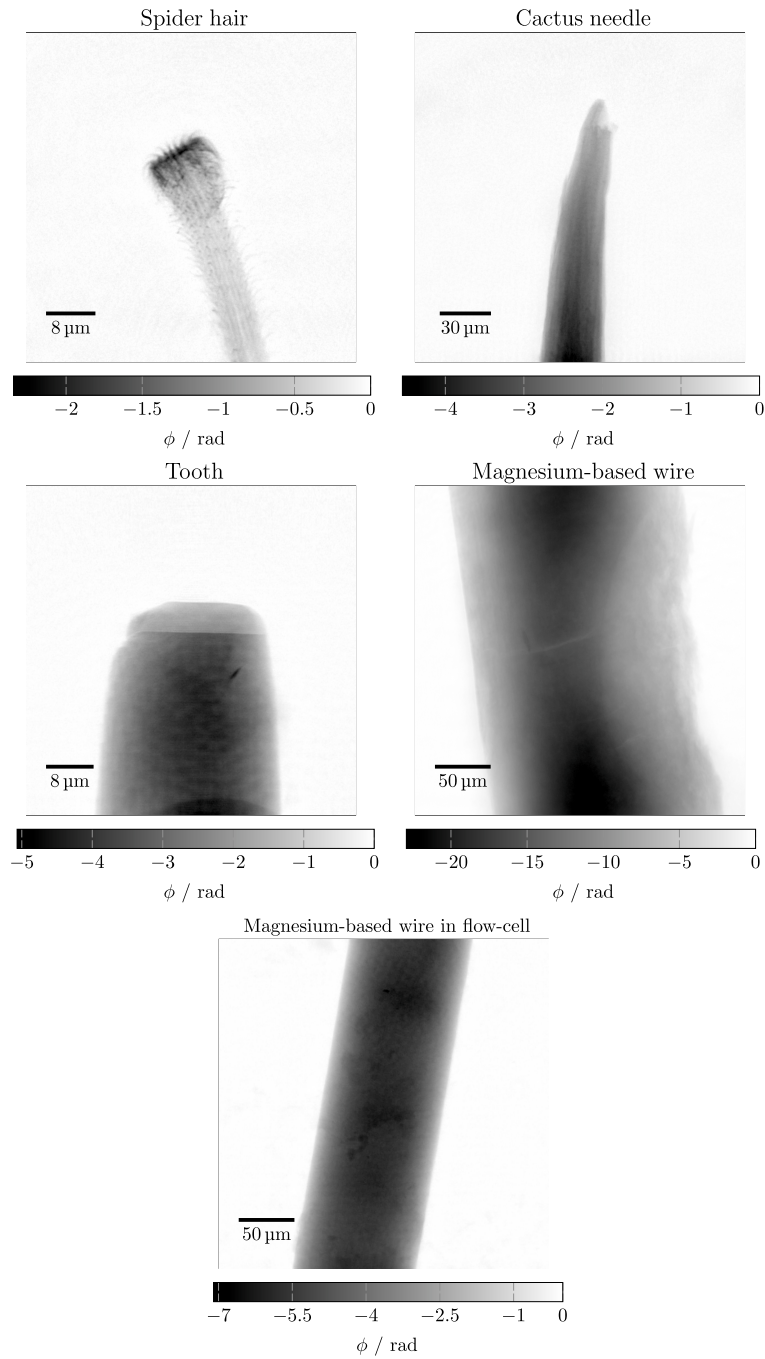
Fig. 6. Experimental data. The images here show phase images reconstructed in full resolution by [28] from single-shot near-field holograms. The reference focus plane was previously manually determined by the method as described in Sec. 3.6. The phase shifting strength (ϕ) is described by the color bars.

3.6. Experimental setup

To evaluate the complete framework, we obtained five experimental datasets at the beamline P05 at PETRA III, located at DESY in Hamburg, operated by Helmholtz-Zentrum Hereon [30–32]. A Fresnel-zone-plate-based setup for NFH as shown in Figure 1 was used [23]. The detector is a scintillator (10 μm Gadox) sCMOS camera (Hamamatsu C12849-101U) with 6.5 μm pixel size at 16 bit image depth and 2048×2048 pixels.

We chose the following samples for our demonstration (Fig. 6): A spider attachment hair [24–26], the tip of a cactus needle, a sample of a human tooth prepared by focused ion beam milling and a partly corroded biodegradable magnesium-based wire [20,41]. Additionally we placed a magnesium-based wire into a flow-cell for in-situ experiments [20], which we filled with ethanol. The measurement parameters for each of the samples are shown in Appendix 5, Table 2.

For each object, we manually measured a guess z_{01}^{est} of the distance z_{01} of the setup as shown in Fig. 1 with an uncertainty of $\Delta_M = \pm 5$ mm. We then determined the reference values z_{01}^0 by manually focusing the object to the correct position. The manual focusing was done by creating a series of reconstructions with different values for z_{01} and choosing the visually sharpest result. We then sampled 201 $\hat{z}_{01}$ in the interval of $[z_{01}^0 - 2\Delta_M, z_{01}^0 + 2\Delta_M]$ and created for each sampling point a reconstruction $\tilde{O}(\hat{z}_{01})$ with the algorithm of Sec. 3.3. The results are used as an input for each focus criterion.

Eventually, we also applied the proposed automatic z_{01} optimization algorithm of Sec. 3.2 on the measured objects with the MFE criterion.

3.7. Analysis of the results

In the following we show the generated focus criteria for each simulated object (cell, triangle, ball) and experimental data (spider hair, cactus needle, tooth, magnesium-based wire, magnesium-based wire in a flow-cell). The generated curves for the focus criteria are shown in Fig. 7 and Fig. 8 and have the same structure. The large curve at the top shows the results of the proposed focus criterion MFE as described in Sec. 3.1. The smaller panels at the bottom show the results for the focus criteria VAR, SPEC, GRA, LAP, ToG and GoG error metrics from literature [1,2,8,29]. For comparison, we normalized each of the criteria values to an interval of [0,1]. We analyzed the generated curves with respect to their applicability to the proposed automatization algorithm in Sec. 3.2. The requirements for focus criteria to be utilizable by our Nelder-Mead-based optimization approach are: (i) All curves exhibit distinct peaks, (ii) the peak direction is consistent within each criterion, (iii) the curves are v-shaped or u-shaped in the uncertainty range around the peak, (iv) to achieve optimal results, the curves should be as smooth as possible. In Table 1, we show the results of the test runs with the proposed automatization algorithm of Sec. 3.2 with the proposed MFE criterion.
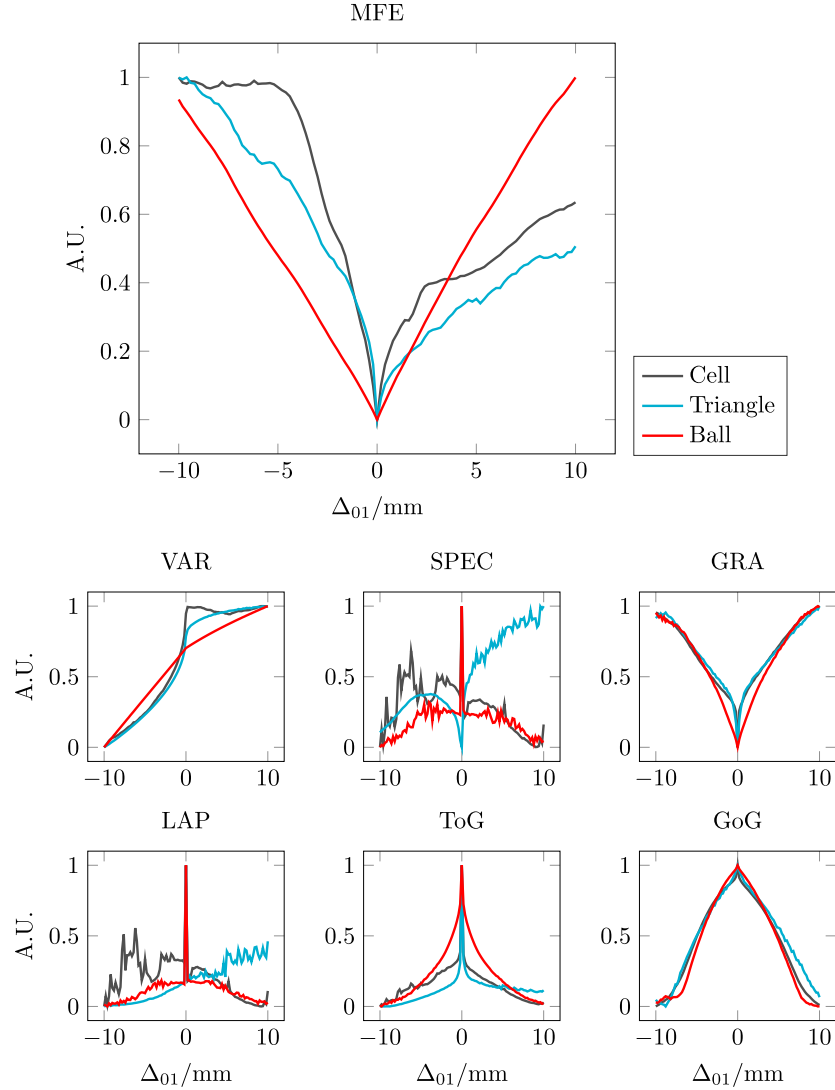
Fig. 7. Focus curves that were generated from simulation data. Three different complex valued objects (Fig. 5) were illuminated by a coherent wavefront of constant intensity. The exit wave-field was defined to be at position $\Delta_{01} = 0$ and then propagated to 201 equidistant sampling points along z_{01}. The respective refractive indices were extracted and projected onto the non-negativity constraint. The result was then used to calculate one sampling point in each criterion as stated in Sec. 3.7. For the MFE criterion, we additionally simulated a hologram of a typical measurement setup, which parameters are given in the Appendix in Sec. A.
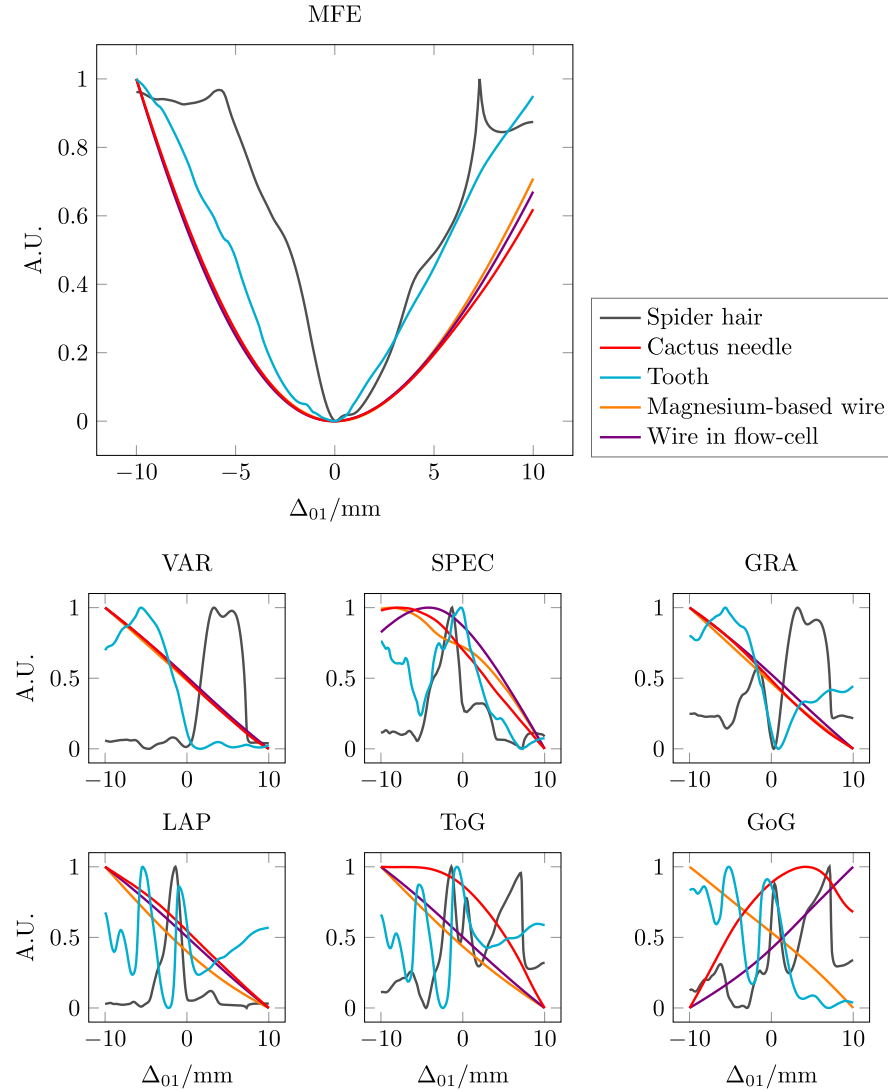
Fig. 8. Focus curves that were generated from experimental data. The respective setup parameters of the experiments are listed in the Appendix in Sec. A and the measured objects are shown in Fig. 6. The reference focus plane was previously manually determined by an optical analysis of the reconstruction results and then chosen as the central point $\Delta_{01} = 0$ for the focus curves. For each curve, 201 equidistant sampling points were generated by performing at each sampling point a reconstruction and using the reconstruction as an input for each criterion. The reconstruction parameters are given in the Appendix in Sec. B.

Table 1. Results of the automatic optimization of z_{01} with the MFE criterion. Upper Table: The measurements are sorted into two types: Depending on the Fresnel number, the measurements needed to be padded to two different array sizes [28]. The probing reconstructions of the Nelder-Mead approach were performed on a 4× down-sampled grid. Bottom Table: We tested the optimization of z_{01} for the objects (i) spider hair, (ii) tooth, (iii) cactus needle, (iv) magnesium-based wire, (v) magnesium-based wire in a flow-cell. The optimization with the Nelder-Mead approach the simplex was initialized with two corner points shown in the second column. The last column shows the required sampling points of the focus curve to find the minimum by shrinking the simplex to a predefined length of 100 μm.

	Type	Full Grid Size / px	Down-sampled Grid Size / px	Time / $\frac{s}{Sample}$
	(1)	14336×14336	3584×3584	16
	(2)	8192×8192	2084×2084	6

Object	Type	Initial Simplex	NM Result	Visually Determined	Required Samples
i	(1)	74.8 mm / 84.8 mm	79.4 mm	79.4 mm	13
ii	(2)	77.9 mm / 87.9 mm	80.9 mm	81.0 mm	11
iii	(1)	281.1 mm / 291.1 mm	284.2 mm	284.2 mm	12
iv	(2)	467.4 mm / 477.4 mm	470.8 mm	470.7 mm	9
v	(2)	324.2 mm / 334.2 mm	329.3 mm	329.3 mm	13

4. Results

4.1. Simulation

In the simulation, the focus curves of the simulated objects differ significantly in their respective shape. The focus curves of MFE, GRA, GoG and ToG show all v-shaped curves with a distinct peak at the in-focus position. Within each criterion, the curves of the different objects are consistently similar while the MFE resulted in less similar curves. In total, the criteria MFE, GRA, GoG and ToG all fulfill the requirements as listed in Sec. 3.7. The VAR criterion produced curves that are smooth but shaped like cubic functions without distinct peaks and therefore only fulfills the low signal-to-noise requirement from Sec. 3.7. For the remaining requirements, the VAR criterion failed to produce satisfying results. The curves of LAP and SPEC have a very distinct peak at the center. However, instead of continuously approaching the extrema from the proximal area, the peaks appear very suddenly and the curves heavily distorted by noise. The LAP criterion hence fails to fulfill three of the four requirements given in Sec. 3.7. The direction of the peaks in the SPEC criterion additionally change between each objects such that the SPEC criterion, in total, does not fulfill any of the given requirements.

4.2. Experimental data

Overall, the produced focus curves of each criterion appear to be heavily influenced by the kind of object measured. Smooth objects like the cactus needle and the two magnesium-based wires produced more smooth curves than objects that contain more structure in the projection images, like the spider hair with many fine details and the tooth, which has step-like structures induced by the focused ion beam. The spider hair and the tooth produced in most of the criteria distinct peaks at the center. Although the peaks are not all aligned in the center, they are still in a plausible range, where the visual analysis does not yield a clear result for the sharpest position. In the range of the overall measurement uncertainty of z_{01}, many of the curves contain very distinct side peaks that are clearly not at the sharpest position. Specifically, the criteria are LAP, ToG and GoG, GRA and SPEC. The VAR criterion behaves similar to the simulation, where the sharpest position only induces a significant gradient in the curve without producing a peak. At the positions, where the objects produced side peaks in all other criteria, the impact on the MFE

criterion is more subtle. The MFE criterion appears to be more robust since these positions produced only minor saddle points in the focus curve.

We also performed a test run to automatically focus the objects of the experimental data with the proposed autofocus algorithm from Sec. 3.2 and the MFE criterion. The algorithm converged successful for all given objects to the visually determined reference z_{01} value. The performance results are shown in Table 1. The Nelder-Mead approach required between 11 and 13 sampling points on the MFE curve, each representing a single reconstruction of $\tilde{O}$ on a down-sampled grid. Depending on the array size, a single reconstruction with the parameters of Table 3 needed between 6 s and 16 s.

5. Summary

We have investigated the autofocus problem of near-field holography data that was acquired under a measurement setup Fig. 1, with respect to an example from X-ray imaging. In Sec. 2 and Fig. 2, it was demonstrated that an inaccurate estimation of the focal-point-to-object-distance z_{01} and the respective Fresnel number yields blurred images with reconstruction artifacts.

In Sec. 3, we proposed the general constraint optimization problem for an automatic optimization of z_{01}. The inverse problem consists of two components: (i) A novel focus criterion based on a model-matching approach, that we called the Model Fit Error (MFE). The MFE metric quantifies the fitting error of the forward model by using the reconstruction, the forward model and the measurements as information. This is in contrast to other error metrics, where usually only the reconstruction result is analyzed, e.g., by a statistical analysis of the pixels. (ii) An ASRM based reconstruction that was parameterized with the distance z_{01}. Both components were embedded into a global optimization problem which we optimized with the Nelder-Mead algorithm, as a gradient-less approach to find a solution for the proposed target function.

In Sec. 4, we compared available error metrics with our proposed MFE approach, with respect to the existence of distinct peaks in the generated curves and smoothness as described in Sec. 3.7. We first compared the criteria with simulation data for different objects (Fig. 5). We created a de-focused wave-field by a simple propagation of a known wave-field. In the simulation, the GRA, GoG, ToG and MFE criteria created all satisfying curves for an application with a Nelder-Mead optimization approach. We further tested our approaches on experimental data of different objects (Fig. 6) that where measured at the beamline P05 at PETRA III, located at DESY in Hamburg. The objects covered interaction strengths from weakly interacting samples which do not exceed phase shifts of 2π to multi-material samples that produce a phase range beyond 6π. We also tested an object under *in-situ* conditions. Here, all statistically based criteria from the literature either failed to produce clear peaks in the center of the focus curve or produced significant side peaks, further limiting the feasible measurement uncertainty for z_{01}. Only our MFE approach exhibited sufficient robustness with simulated as well es with experimental data to be used in a Nelder-Mead-based optimization algorithm.

We have demonstrated that the proposed autofocus algorithm for near-field holography is able to focus a wide range of real objects and experimental setup conditions. The autofocus problem is also not only relevant for this specific setup but also extends to other microscopy setups and reconstruction algorithms that use the Fresnel free-space propagation in the forward model. The proposed algorithm can be adapted for any hyperparameter that is part of the Fresnel number in the forward model of an experimental setup, including propagation distance, energy, pixel size and others. This flexibility and the demonstrated robustness makes the method highly useful for *in-situ/operando* studies. The proposed model-matching-error-based focus criterion yields a superior robustness compared to the statistical analysis of reconstructed images. The optimization only needs to be performed once per measurement configuration. With only a few minutes to converge to an optimum, the computation time is reasonably small for an application during experiments. This work is a step further towards simplified and automatized processing of

large amounts of holographic data sets, which could enable an online reconstruction to monitor and control the state of dynamic measurements.

Appendix

A. Measurement parameters

Table 2. Parameters for the measurement setup as shown in Fig. 1, the calculated effective Fr and the exposure time *t*.

Object	Energy	z_{01}	z_{02}	Fr	t
Spider hair	11.0 keV	79.4 mm	19.661 m	7.790×10^{-5}	1.0 s
Cactus needle	17.0 keV	284.1 mm	19.652 m	4.347×10^{-4}	0.8 s
Tooth	17.0 keV	81.0 mm	19.652 m	1.231×10^{-4}	0.8 s
Magnesium-based wire	11.0 keV	470.8 mm	19.661 m	4.678×10^{-4}	1.5 s
Wire in flow-cell	11.0 keV	329.3 mm	19.914 m	3.165×10^{-4}	1.3 s
Simulation	11.0 keV	100.0 mm	20.000 m	9.331×10^{-5}	-

B. Reconstruction parameters of $\tilde{O}$

Table 3. Reconstruction parameters for the iterative reconstruction algorithm in Sec. 3.3, that were used to reconstruct $\tilde{O}^*(\hat{z}_{01})$. Applied stepwise from left to right. The filter $\tilde{O}$ values are given in Full Width at Half Magnitude (FWHM) for real and imaginary parts in the form of $FWHM_{real}/FWHM_{imag}$. The momentum variance is given as FWHM in pixels where $\sigma = FWHM/2.35$.

Iterations		700	300	500
Down-sampling	$S_\downarrow$	16×	4×	4×
Update Rate	η	0.9	1.1	1.1
Momentum Weight	γ	1.0	1.0	1.0
Momentum Variance	σ	8	16	16
L_2 Weight	β	10.0	10.0	1.0
Filter $\tilde{O}$		2.0/0.0	2.0/8.0	2.0/8.0

References

1. P. Langehanenberg, B. Kemper, D. Dirksen, *et al.*, "Autofocusing in digital holographic phase contrast microscopy on pure phase objects for live cell imaging," Appl. Opt. **47**(17), D176–D182 (2008).

2. Y. Zhang, H. Wang, Y. Wu, *et al.*, "Edge sparsity criterion for robust holographic autofocusing," Opt. Lett. **42**(19), 3824–3827 (2017).
3. M. Liebling and M. Unser, "Autofocus for digital Fresnel holograms by use of a Fresnelet-sparsity criterion," J. Opt. Soc. Am. A **21**(12), 2424–2430 (2004).
4. Y. Sun, S. Duthaler, and B. J. Nelson, "Autofocusing in computer microscopy: selecting the optimal focus algorithm," Microscopy Res. Tech. **65**, 139–149 (2004).
5. L. Firestone, K. Cook, K. Culp, *et al.*, "Comparison of autofocus methods for automated microscopy," Cytometry **12**, 195–206 (1991).
6. M. Bravo-Zanoguera, B. v. Massenbach, A. L. Kellner, *et al.*, "High-performance autofocus circuit for biological microscopy," Rev. Sci. Instruments **69**(11), 3966–3977 (1998).
7. F. C. Groen, I. T. Young, and G. Ligthart, "A comparison of different focus functions for use in autofocus algorithms," Cytometry **6**, 81–91 (1985).
8. P. Memmolo, C. Distante, M. Paturzo, *et al.*, "Automatic focusing in digital holography and its application to stretched holograms," Opt. Lett. **36**(10), 1945–1947 (2011).
9. J. R. Fienup, "Phase retrieval algorithms: a personal tour [Invited]," Appl. Opt. **52**(1), 45 (2012).
10. R. P. Millane, "Phase retrieval in crystallography and optics," J. Opt. Soc. Am. A **7**(3), 394 (1990).
11. D. R. Luke, J. V. Burke, and R. G. Lyon, "Optical Wavefront Reconstruction: Theory and Numerical Methods," SIAM Rev. **44**(2), 169–224 (2002).
12. L. Taylor, "The phase retrieval problem," IEEE Trans. Antennas Propagat. **29**(2), 386–391 (1981).
13. Y. Shechtman, Y. C. Eldar, O. Cohen, *et al.*, "Phase Retrieval with Application to Optical Imaging: A contemporary overview," IEEE Signal Processing Magazine **32**(3), 87–109 (2015).
14. D. Gabor, "A New Microscopic Principle," Nature **161**(4098), 777–778 (1948).
15. D. L. Misell, "An examination of an iterative method for the solution of the phase problem in optics and electron optics: I. Test calculations," J. Phys. D: Appl. Phys. **6**(18), 2200–2216 (1973).
16. P. Cloetens, W. Ludwig, J. Baruchel, *et al.*, "Holotomography: Quantitative phase tomography with micrometer resolution using hard synchrotron radiation x rays," Appl. Phys. Lett. **75**(19), 2912–2914 (1999).
17. J. Hagemann, A.-L. Robisch, D. R. Luke, *et al.*, "Reconstruction of wave front and object for inline holography from a set of detection planes," Opt. Express **22**(10), 11552–11569 (2014).
18. J. Hagemann, M. Vassholz, H. Hoeppe, *et al.*, "Single-pulse phase-contrast imaging at free-electron lasers in the hard X-ray regime," J. Synchrotron Rad. **28**(1), 52–63 (2021).
19. S. Meyer, A. Wolf, D. Sanders, *et al.*, "Degradation Analysis of Thin Mg-xAg Wires Using X-ray Near-Field Holotomography," Metals **11**, 1422 (2021).
20. J. Reimers, H. C. Trinh, B. Wiese, *et al.*, "Development of a Bioreactor-Coupled Flow-Cell Setup for 3D In Situ Nanotomography of Mg Alloy Biodegradation," ACS Appl. Mater. Interfaces **15**(29), 35600–35610 (2023).
21. F. Sun, X. He, X. Jiang, *et al.*, "Advancing knowledge of electrochemically generated lithium microstructure and performance decay of lithium ion battery by synchrotron X-ray tomography," Materials Today **27**, 21–32 (2019).
22. Z. Zhang, K. Dong, K. A. Mazzio, *et al.*, "Phase Transformation and Microstructural Evolution of CuS Electrodes in Solid-State Batteries Probed by In Situ 3D X-Ray Tomography," Advanced Energy Materials **13**, 2203143 (2022).
23. S. Flenner, A. Kubec, C. David, *et al.*, "Hard X-ray nano-holotomography with a Fresnel zone plate," Opt. Express **28**(25), 37514–37525 (2020).
24. D. T. Roscoe and G. Walker, "The adhesion of spiders to smooth surfaces," Bull. Br.Arachnol. Soc. (1991).
25. C. F. Schaber, S. Flenner, A. Glisovic, *et al.*, "Hierarchical architecture of spider attachment setae reconstructed from scanning nanofocus X-ray diffraction data," J. R. Soc. Interface. **16**(150), 20180692 (2019).
26. S. Niederegger and S. N. Gorb, "Friction and adhesion in the tarsal and metatarsal scopulae of spiders," J Comp Physiol A **192**(11), 1223–1232 (2006).
27. F. Wittwer, J. Hagemann, D. Brückner, *et al.*, "Phase retrieval framework for direct reconstruction of the projected refractive index applied to ptychography and holography," Optica **9**(3), 295–302 (2022).
28. J. Dora, M. Möddel, S. Flenner, *et al.*, "Artifact-suppressing reconstruction of strongly interacting objects in X-ray near-field holography without a spatial support constraint," Opt. Express **32**(7), 10801–10828 (2024).
29. N. Hurley and S. Rickard, "Comparing measures of sparsity," IEEE Trans. Inform. Theory **55**(10), 4723–4741 (2009).
30. M. Ogurreck, F. Wilde, J. Herzen, *et al.*, "The nanotomography endstation at the PETRA III Imaging Beamline," J. Physics: Conference Series **425**(2), 182002 (2013).
31. A. Haibel, M. Ogurreck, F. Beckmann, *et al.*, "Micro- and nano-tomography at the GKSS Imaging Beamline at PETRA III," in *Developments in X-Ray Tomography VII*, S. R. Stock, ed. (SPIE, 2010).
32. A. Haibel, F. Beckmann, T. Dose, *et al.*, "Latest developments in microtomography and nanotomography at PETRA III," Powder Diffr. **25**(2), 161–164 (2010).
33. J. Dora, S. Flenner, A. Lopes Marinho, *et al.*, "A Python framework for the online reconstruction of X-ray near-field holography data," zenodo, (2024) https://doi.org/10.5281/zenodo.8349364.
34. D. Paganin, *Coherent X-Ray Optics* (Oxford University Press, 2006).
35. A. Suzuki, S. Furutaku, K. Shimomura, *et al.*, "High-resolution multislice x-ray ptychography of extended thick objects," Phys. Rev. Lett. **112**(5), 053903 (2014).
36. T. M. Godden, R. Suman, M. J. Humphry, *et al.*, "Ptychographic microscope for three-dimensional imaging," Opt. Express **22**(10), 12513–12523 (2014).

37. N. Chen, C. Wang, and W. Heidrich, "∂H: Differentiable Holography," Laser Photonics Rev. **17**, 2200828 (2023).
38. H. Zhu, Z. Liu, Y. Zhou, *et al.*, "DNF: diffractive neural field for lensless microscopic imaging," Opt. Express **30**(11), 18168 (2022).
39. J. A. Nelder and R. Mead, "A Simplex Method for Function Minimization," The Computer Journal **7**(4), 308–313 (1965).
40. J. C. Lagarias, J. A. Reeds, M. H. Wright, *et al.*, "Convergence Properties of the Nelder–Mead Simplex Method in Low Dimensions," SIAM J. Optim. **9**(1), 112–147 (1998).
41. B. Zeller-Plumhoff, H. Helmholz, F. Feyerabend, *et al.*, "Quantitative characterization of degradation processes in situ by means of a bioreactor coupled flow chamber under physiological conditions using time-lapse SRμCT," Materials and Corrosion **69**, 298–306 (2018).